LBNL-44804
Preprint

ERNEST ORLANDO LAWRENCE
BERKELEY NATIONAL LABORATORY

On Fluid Flow and Mineral Alteration in Fractured Caprock of Magmatic Hydrothermal Systems

Tianfu Xu and Karsten Pruess

Earth Sciences Division

February 2000

Submitted to
Journal of Geophysical Research

DISCLAIMER

LBNL-44804

On Fluid Flow and Mineral Alteration in Fractured Caprock of Magmatic Hydrothermal Systems

Tianfu Xu and Karsten Pruess

Earth Sciences Division, Lawrence Berkeley National Laboratory, University of California, Berkeley, CA 94720.

Submitted to *Journal of Geophysical Research*

February 2000

This work was supported by the Laboratory Directed Research and Development Program of the Ernest Orlando Lawrence Berkeley National Laboratory, and by the Assistant Secretary for Energy Efficiency and Renewable Energy, Office of Geothermal and Wind Technologies, of the U.S. Department of Energy, under Contract No. DE-AC03-76SF00098.

On Fluid Flow and Mineral Alteration in Fractured Caprock of Magmatic Hydrothermal Systems

Tianfu Xu and Karsten Pruess

Earth Sciences Division, Lawrence Berkeley National Laboratory, University of California, Berkeley, CA 94720.

Abstract. Geochemical evolution in hydrothermal fractured rock systems occurs through a complex interplay of multi-phase fluid and heat flow, and chemical transport processes. On the basis of previous work we present here simulations of reactive hydrothermal flow that include: (1) detailed fracture-matrix interaction for fluid, heat and chemical constituents, (2) gas phase participation in multiphase fluid flow and geochemical reactions, (3) the kinetics of fluid-rock chemical interaction, and (4) heat effects on thermophysical and chemical properties and processes. The present study uses, as an example, water and gas chemistry data from the hydrothermal system in Long Valley Caldera, California, but it is not intended to be specific to any particular geothermal field site. The flow system studied is intended to capture realistic features of fractured magmatic hydrothermal systems. The "numerical experiment" provides useful insight into process mechanisms such as fracture-matrix interaction, liquid-gas phase partitioning, and conditions and parameters controlling water-gas-rock interactions in a hydrothermal setting. Results indicate that vapor-CO_2 discharge through fractures in the rock mass causes strong alteration of primary minerals, and lead to the formation of secondary minerals, resulting in changes in physical and chemical properties of the system.

1. Introduction

The interaction between hydrothermal fluids and the rocks through which they migrate alters the earlier formed primary minerals and leads to the formation of secondary minerals, resulting in changes in physical and chemical properties of the system. These processes have received increasing attention by investigators of hydrothermal alteration, and engineers concerned with geothermal energy exploration and development. Understanding reactive fluid flow and transport under a hydrothermal regime is a challenging task because of the complexity of multiphase fluid flow, water-gas-rock and fracture-matrix interaction mechanisms, difficulties dealing with the heterogeneous physical and chemical properties of the medium, and the highly nonlinear nature of mathematical equations governing these processes.

The traditional analysis approach of geochemical evolution and rock alteration involves separating fluid flow from chemical transport, using geochemical batch models such as those by *Parkhurst et al.* [1980], *Reed* [1982], *Spycher and Reed* [1989], *Wolery* [1992], and *Moller* [1998]. However, the geochemical evolution in hydrothermal fractured rock systems occurs through a complex interplay of multi-phase fluid and heat flow, and chemical transport processes. Recently there has been a growing interest in combining these disciplines in order to simulate reactive chemical transport in porous media [*Steefel and Lasaga*, 1994; *Friedly and Rubin*, 1992; *White*, 1995; *White and Christenson*, 1998; and *White and Mroczek*, 1998].

Using this prior work as a foundation upon which to build, we consider the following processes in this study: (1) detailed fracture-matrix interaction for fluid, heat

and chemical constituents; (2) gas phase participation in multiphase fluid flow and geochemical reactions; (3) the kinetics of fluid-rock chemical interaction, and (4) heat effects on thermophysical and chemical properties and processes, which include water and CO_2 partitioning between liquid and gas phases, temperature-dependent phase density and viscosity, and thermodynamic chemical equilibrium and kinetic rate constants. In prior studies, most investigators assume fluid-rock interactions involve local equilibrium [*Friedly and Ruben*, 1992; *White*, 1995; *White and Christenson*, 1998; and *White and Mroczek*, 1998]. This assumption is justified under certain conditions such as in the hot areas of the reservoir and where geologic time frames are involved, but is generally not valid under conditions of low temperatures and short time periods. Furthermore, multi-mineralic systems generally have a smaller surface area for a given mineral, a factor that favors disequilibrium behavior [*Bolton et al.*, 1999].

The range of problems concerning the interaction of hydrothermal fluids with rocks is very broad. In the present study, we confine our attention to the evolution of geothermal fields associated with magmatic activity, such as are encountered in the Long Valley Caldera (LVC), California [*Sorey*, 1985; *White and Peterson*, 1991; *Kennedy*, personal comm.] and in the Taupo Volcanic Zone, New Zealand [*White and Christenson*, 1998]. In the hydrothermal fluids in these areas, water vapor and CO_2 are the dominant gas phase constituents. The present study uses, as an example, water and gas chemistry data from the hydrothermal system in the LVC [*Sorey*, 1985; *White and Peterson*, 1991], but it is not intended to be specific to any particular geothermal field site. The flow system studied in this paper is intended to capture realistic features of hydrothermal systems such as the LVC.

To understand the intricate web of interactions of fluids, aqueous and gaseous chemical constituents, and rock forming minerals, we need a computational simulation tool that works like a key for unlocking the mysteries of natural geochemical systems. For this purpose, we first present TOUGHREACT, a comprehensive non-isothermal multiphase fluid flow and geochemical transport computer model which was developed by *Xu and Pruess* [1998]. If in the simulations it were possible to (a) achieve a realistic representation of all important physical and chemical processes, and (b) utilize realistic hydrogeologic and chemical parameters for the hydrothermal system under study, then the outcome of the numerical simulations should match field observations. Because of numerous uncertainties and lack of sufficiently detailed characterization data, such an ambitious goal cannot be completely reached at present. In undertaking the simulations presented in this paper, we were mindful of these limitations and have pursued more modest objectives. Our simulation should be thought of as a "numerical experiment" which permits a detailed view of the dynamical interplay between coupled hydrologic, thermal, and chemical processes, albeit in an approximate fashion. A critical evaluation and discussion of modeling results on their own terms can provide useful insight into process mechanisms.

2. Numerical method

2.1 Model description

Our present study is carried out by means of numerical simulations of non-isothermal reactive chemical transport using the TOUGHREACT model [*Xu and Pruess*, 1998; and *Xu et al.*, 1999b]. This model was developed by introducing reactive chemistry into the framework of the existing multi-phase fluid and heat flow code TOUGH2 [*Pruess*, 1991]. The flow and transport in geologic media are based on space discretization by means of integral finite differences [*Narasimhan and Witherspoon*, 1976]. An implicit time-weighting scheme is used for flow, transport, and geochemical reaction. TOUGHREACT uses a sequential iteration approach similar to *Yeh and Tripathi* [1991], *Walter et al.* [1994], and *Xu et al.*, [1999a], which solves the transport and the reaction equations separately. The chemical transport equations are solved independently for each chemical component. The system of chemical reaction equations is solved on a grid-block basis by a Newton-Raphson iterative method similar to that of *Parkhurst* [1980], *Reed* [1982], and *Wolery* [1992]. Full details on numerical methods are given in *Xu and Pruess* [1998].

The model can be applied to one-, two-, or three-dimensional porous and fractured media with physical and chemical heterogeneity. The model can accommodate any number of chemical species present in liquid, gas and solid phases. A wide range of subsurface thermo-physical-chemical processes is considered. Major processes for fluid and heat flow are: (1) fluid flow in both liquid and gas phases occurs under pressure and

gravity forces; (2) capillary pressure effect for the liquid phase; (3) heat flow by conduction, convection and diffusion. Transport of aqueous and gaseous species by advection and molecular diffusion is considered in both liquid and gas phases. Aqueous chemical complexation and gas (CO_2) dissolution/exsolution are considered under the local equilibrium assumption. Mineral dissolution/precipitation can proceed either subject to local equilibrium or kinetic conditions. The equations used to model fluid and heat flow, chemical transport and reactions are given in Appendix 1.

2.2. Simplifying approximations

Temporal changes in porosity and permeability can modify fluid flow. For a "fully coupled" model of reactive fluid flow and transport, this "feedback" coupling is important [*Raffensperger*, 1996]. However, its inclusion results in a rather large computational penalty. This is the primary reason why we neglect effects of changes in porosity and permeability on fluid flow. Another reason arises from the complex relationship between porosity and permeability. The porosity-permeability correlation depends on many factors such as pore size distribution, pore shape, and connectivity [*Verma and Pruess*, 1988]. Because of the complexity of natural geologic media, a simple functional porosity-permeability relationship is most likely not realistically attainable [*Raffensperger*, 1996]. Thus, by neglecting porosity and permeability change, we obtain a steady-state flow condition, which greatly simplifies the problem and saves computing time, and makes it possible to consider the geochemistry in greater detail. Furthermore, in our modeling we monitor porosity change, which is calculated directly once mineral volume fractions have been determined, although we do not allow it to affect fluid flow.

Finally, neglecting the feedback effect of porosity and permeability changes on fluid flow is certainly justifiable for a limited time span, during which such changes remain small. The modeling results presented later in this paper indicate that after 1000-year simulation, changes in porosity are less than 0.8 % (see Figure 10f).

In the present work, the following are also neglected: (1) compaction and thermal mechanics, such as micro-fracturing by thermal stress and hydro-fracturing by thermal expansion of pore fluid; (2) the effect of chemical concentration changes on fluid thermophysical properties such as density and viscosity which are otherwise primarily dependent on pressure and temperature; (3) the enthalpy due to chemical reactions.

3. Conceptual model

The present simulation study is not specific to any site. However, some data such as reservoir conditions, and water and gas chemistry are taken from the hydrothermal system in Long Valley Caldera (LVC), a 450 km^2 elliptical depression located along the eastern front of the Sierra Nevada in east-central California [*Sorey*, 1985; *White and Peterson*, 1991; and *Kennedy*, personal comm.]. Many hot springs in and around LVC occur along north to northwest trending normal faults, and are derived from hydrothermal reservoirs. Hot water is transported upward along fault systems into shallow aquifers [*Sorey*, 1985; *White and Peterson*, 1991]. In these aquifers, the hydrothermal fluids mix with varying proportions of cold meteoric water before discharging in the hot springs. The present LVC hydrothermal system has been active for perhaps 40, 000 years [*Flexser*, 1991].

For the sake of simplification and interpretation of results, we consider an idealized fractured rock with a set of plane, and parallel vertical fracture zones (faults) of equal aperture (0.1 m) and spacing (3.5 m). Because of the symmetry of this fractured rock, only one column of matrix blocks needs to be modeled (Figure 1). We simulated a vertical column extending from the atmosphere (top boundary) through the fracture-matrix system and extending to the hydrothermal reservoir (bottom boundary). The depth of the hydrothermal reservoir varies from site to site. For example, according to the data presented in *White and Peterson* [1991] for the LVC, the reservoir depth varies from several tens of meters to near 1000 meters. In this study, we use a single depth of 280 m for simplicity. A 1-m-thick vertical slice is modeled, where a total depth of 280 m is discretized into 56 layers of 5 m thickness. The fracture is considered as one model grid zone. The rock matrix is further discretized into 6 grid zones with permeability and reactive surface area decreasing away from the fracture. A thermal conductivity of 2.1 W/m°C, a specific heat of 920 J/kg°C, and an aqueous chemical diffusion coefficient of 1×10^{-10} m^2/s are used. Other parameters for the fracture and matrix are listed in Table 1. The top atmosphere and bottom hydrothermal reservoir boundaries are modeled as constant pressure boundaries with properties shown in Figure 1. At a depth of 87.5 m the rising hot water mixes with the shallow cold meteoric aquifer water. The cold water (11 °C) recharge is assumed to occur only in the fracture grid block at a rate of 3×10^{-5} kg/s, and is treated as a source term for fluid, heat and chemical constituents, the concentrations of which are given in Table 2. The bottom reservoir is assigned the same medium thermo-physical properties as the fracture zone.

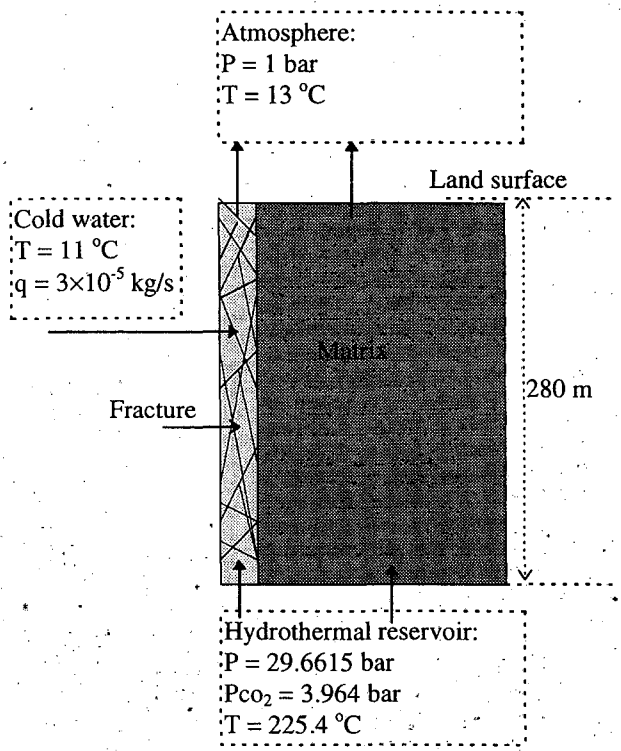

Fig. 1. Vertical 2-D section model for hydrothermal fluid flow and rock alteration in a fractured rock.

Table 1. Some parameters used in the simulation for the fracture-matrix system

medium	fracture	matrix	matrix	matrix
symbol	F	M1	M2	M3, M4, M5, M6
grid spacing (m)	0.05	0.1	0.15	0.2, 0.3, 0.4, 0.55
permeability (m^2)	1×10^{-12}	1×10^{-14}	1×10^{-15}	1×10^{-16}
parameters for relative permeability and capillary pressure functions [*van Genuchten*, 1980]:				
λ	0.457	0.457	0.457	0.457
S_{lr}	0.15	0.20	0.30	0.40
S_{ls}	1.0	1.0	1.0	1.0
P_0(pa)	6.195×10^{3}	6.195×10^{4}	1.959×10^{5}	6.195×10^{5}
porosity	0.5	0.1	0.09	0.08
reactive surface reduction factor	1	0.2	0.05	0.01

The reservoir chemical composition is based on data reported by White and Peterson [1991]. The concentrations of major chemical species in samples at various wells are in general similar, and we arbitrarily choose data from well RDO-8 (Table 2) for our simulation. CO_2 is the dominant gaseous species in the hydrothermal system, and its partial pressures range from 1 to 9 bar. We use an intermediate partial pressure value of approximately 4 bars. H_2S gas is also present with a partial pressure of approximately 0.02 bar. Thus the dominant the sulfur species could be sulfides H_2S and HS^-. The measured aqueous chemical data indicate, however, the sulfate species is the dominant form. *White and Peterson* [1991] predicts that sulfur speciation would approach redox equilibrium in approximately 10^3-10^4 years, using data for LVC and the kinetic rate equation of *Ohmoto and Lasaga* [1982]. Time scales for speciation could exceed the fluid residence time in fractured rock as hydrothermal fluids move to the land surface. Therefore, neglecting the sulfur redox process in this study may be justified for our objectives. The cold recharge water chemical composition is taken from *Sorey* [1985] for cold Big Springs of LVC (Table 2) which is assumed to be representative of the shallow aquifer meteoric water. The initial fracture-matrix system is assumed to be liquid-water saturated. Thermodynamic equilibrium constants are taken from the EQ3/6 database [*Wolery*, 1992].

Table 2. Aqueous chemical concentrations (mol/kg H_2O) of hot reservoir water and cold meteoric water used for the simulation study.

Component	hot water	cold water
Ca^{2+}	$4.49x10^{-4}$	$1.27x10^{-4}$
Mg^{2+}	$1.44x10^{-5}$	$2.43x10^{-4}$
Na^{+}	$1.65x10^{-2}$	$1.00x10^{-3}$
K^{+}	$1.23x10^{-3}$	$1.00x10^{-4}$
HCO_3^-	$7.92x10^{-3}$	$1.21x10^{-3}$
SO_4^{2-}	$1.86x10^{-3}$	$8.33x10^{-5}$
Al^{3+}	$1.00x10^{-6}$	$1.00x10^{-6}$
$SiO_2(aq)$	$4.61x10^{-3}$	$9.65x10^{-4}$
Cl^-	$7.41x10^{-3}$	$1.61x10^{-4}$
pH	6.6	6.8
T (°C)	225	11

The caprock mineral composition is highly variable in geothermal reservoirs. For the purpose of our study, we chose an initial rock mineral assemblage as listed in Table 3 throughout the column, which is based on the studies carried out by *Steefel and Lasaga* [1994] and *White and Christenson* [1998]. The dissolution of the primary minerals proceeds subject to kinetic controls. The kinetic rate law used is given in Eq. A.1 (in Appendix 1). The temperature-dependent kinetic rate constants are calculated from Eq. A.2, and the required parameters, k_{25} and E_a, are also given in Table 3. The initial specific surface areas given in Table 3 must be multiplied by the reactive surface area factor given in Table 1 for each different matrix grid zone, in order to take into account the fact that reactive surface areas may decrease from the fractures towards the interior of the rock matrix. With time, the surface areas change in complex ways. In this study, however, we simply relate the surface areas of the primary minerals at some time to the mineral volume fraction by, $A = A_0 V_f / V_f^0$, where A_0, and V_f^0 are the initial surface area and volume fraction of a primary mineral, respectively. The precipitation of secondary

minerals (also given in Table 3) is represented using the same kinetic expression as that for dissolution. However, several aspects regarding precipitation are different, including nucleation, crystal growth and Ostwald ripening processes, as well as the calculation of the reactive surface area [*Steefel and van Capellen*, 1990]. To simplify the description of precipitation kinetics, a constant reactive surface area of 0.01 m^2 per one dm^3 (cubic decimeter) medium is used for the entire simulation time. Kinetic rates of precipitation depend on the activities of reactants supplied by dissolution. Because reactive surface areas cover a wide range of values, two additional runs were performed by changing the surface areas given in Table 3, to analyze the sensitivity.

Table 3. Initial caprock mineral volume fractions (with $V_f > 0$ where V_f is mineral volume fraction) and secondary mineral phases ($V_f = 0.0$) formed in the simulation. The kinetic rate law used is given in Eq. A.1 (in Appendix 1) using two exponential parameters μ and n setting equal to one (first order kinetics). Rate constants are calculated from Eq. A.2, and kinetic constant at 25 °C (k_{25}) and activation energy (E_a) are taken from *Steefel and Lasaga* [1994], and *Johnson et al.* [1998].

Mineral	Chemical composition	Volume (%)	Surface area (m^2/dm^3 medium)	k_{25} (moles $m^{-2}s^{-1}$)	E_a (KJ/mol)
Primary:					
quartz	SiO_2	35	0.035	$4.30x10^{-14}$	75.00
cristobalite	SiO_2	23	0.023	$3.16x10^{-13}$	69.08
K-feldspar	$KAlSi_3O_8$	30	0.03	$1.00x10^{-12}$	67.83
albite	$NaAlSi_3O_8$	2	0.002	$1.00x10^{-12}$	67.83
anorthite	$CaAl_2Si_2O_8$	2	0.002	$1.00x10^{-12}$	67.83
porosity		8	----	----	----
total		100	----	----	----
Secondary:					
kaolinite	$Al_2Si_2O_5(OH)_4$	0	0.01	$1.00x10^{-13}$	62.76
muscovite	$KAl_3Si_3O_{10}(OH)_2$	0	0.01	$1.00x10^{-14}$	58.58
pyrophyllite	$Al_2Si_4O_{10}(OH)_2$	0	0.01	$1.00x10^{-13}$	62.76
paragonite	$NaAl_3Si_3O_{10}(OH)_2$	0	0.01	$1.00x10^{-14}$	58.58
calcite	$CaCO_3$	0	0.01	$1.00x10^{-11}$	41.87
Amorphous silica	SiO_2	0	0.01	$7.94x10^{-13}$	62.80

The simulation is run for 1000 years. Initially, we limit the simulation only to fluid and heat flow until a steady-state is attained. Then we simulate chemical transport and fluid-rock interactions using the steady-state fluid and heat flow as the initial condition. Modeling the transport of a chemically reactive multi-component fluid is computationally intensive, and requires that a balance be struck between fluid and chemical complexity and calculation time. The described two-step approach can significantly save on computational time and give a detailed description of geochemical evolution of the system. Despite our use of a two-step approach, our model is fully capable of simulating both flow and reactive transport at the same time. In addition, the interpretation of results is easier when flow is decoupled from reactive transport. Although we only consider an idealized fractured rock, generally any fracture geometry can be considered by our model. Furthermore, we should point out that CO_2 consumed by mineral precipitation such as calcite is assumed not to affect its partial pressure and then fluid flow. If at the bottom boundary (geothermal reservoir) the partial pressure remains constant as in the case simulated in this paper, this assumption is justified. A 1-D vertical column is tested first with the bottom and top boundary conditions as shown in Figure 1. The effect of CO_2 consumed by calcite precipitation on fluid flow is negligible in this kinetically-controlled chemical system. Most calcite precipitation occurs close to the bottom reservoir. CO_2 consumed by calcite precipitation is replenished by enhanced physical transport processes from the reservoir.

4. Results

4.1. Fluid flow and heat transfer

At the start of the simulation, hot two-phase fluids (liquid and gas) move up from the high pressure hydrothermal reservoir toward the land surface. A steady-state fluid and heat flow condition for the entire fracture-matrix system is reached after approximately 200 years. To facilitate the analysis of the spatial distribution of variables, contour plots of the steady-state fluid and heat flow condition are displayed to give a general picture. These plots are complemented with graphs showing the variation of various parameters along vertical profiles, to resolve details of their variations. The contour plots of steady-state liquid water saturation and temperature are presented in Figure 2. The tight rock matrix (grid zones M3-7, Table 1) is almost water saturated due to high capillary suction effect, and therefore gas (water vapor and CO_2) access to the matrix is impeded. At a depth of 87.5 m, the matrix is highly saturated with water. This is because the fracture receives a lateral cold water recharge, some of which is immediately imbibed by the matrix, and the remaining fluid flows upward along the fracture. High liquid saturation close to the land surface is due to fluid cooling and heat loss to the atmosphere (13 °C). The temperature distribution is quite uniform between fracture and matrix, because conduction is the dominant heat transfer process and the two media are almost homogeneous in terms of their thermal properties. Figure 3a gives a more detailed evolution along the vertical fracture zone. The liquid saturation decreases slightly with increasing elevation until a depth of 87.5 m, where it increases dramatically due to the

cold water recharge, it then again decreases slightly, and finally liquid saturation increases at the top due to fluid and heat discharge to the land surface. The relative liquid flow rate (R_l) shown in Figure 3a, normalized to the total (fracture and matrix) land surface discharge (5.49×10^{-5} kg/s), slightly decreases from the bottom like the liquid saturation. After the cold water recharge R_L dramatically increases from 24% to 87%. Finally 80% of the liquid discharge is from the narrow fracture at the land surface (16.4% from M1). Even though the mixing ratio of hot water to cold water is 1:2.6 (by mass), the temperature decreases only slightly (from 178 to 162 °C). This suggests that the rock matrix has a strong thermal buffering capability. In addition, nearly all of the total CO_2 output (2.46×10^{-6} kg/s) discharges from the fracture. Figure 3b shows that temperature gradually falls with elevation, then drops suddenly when mixing with the cold water (11 °C) occurs. When close to the land surface, temperature decreases very rapidly due to heat loss to the atmosphere.

Now we return to the fracture-matrix interaction profile (Figure 4a). Above the cold water recharge horizon, the high liquid water flux goes to the matrix (M1) from the fracture (F), and then immediately returns to the fracture at the upper grid. Closer to the land surface, liquid water again flows into the matrix. Liquid water flow in the matrix gradually decreases away from the fracture (Figure 4b).

We turn our attention to the gas phase. Figure 5 shows the contour plots of total gas phase pressure (P_g) and CO_2 partial pressure (P_{CO_2}). In general, P_g gradually decreases from the bottom to the top. P_{CO_2} generally also decreases from the bottom to the top but a peak value appears after mixing with cold water. The sharp increase of

P_{CO_2} can be clearly seen from Figure 6a. This is because (1) gas saturation is dramatically decreased due to the cold water recharge, (2) cooling and condensation causes CO_2 to become the dominant gas phase constituent, (3) CO_2 solubility in water has a minimum at 160 °C [*Battistelli et al.*, 1997], the temperature in the mixing zone, and (4) it is assumed the mixing occurs at one narrow location. Almost 100% of the gas flows through the fracture. Figure 6b shows that P_{CO_2} contributes approximately 13% to the gas phase pressure below the cold water horizon. Above that horizon, P_{CO_2} contributes 45% of the gas pressure. After a local minimum when P_{CO_2} decreases to 34%, the P_{CO_2} contribution to the gas phase increases, and at the land surface the gas phase is almost entirely made up of CO_2.

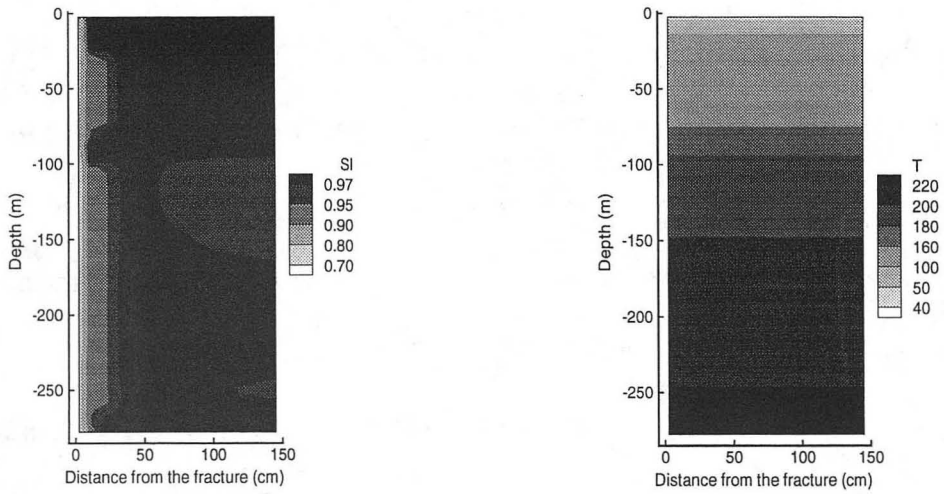

Fig. 2. Liquid saturation (a) and temperature (b, in °C) in the fracture-matrix system.

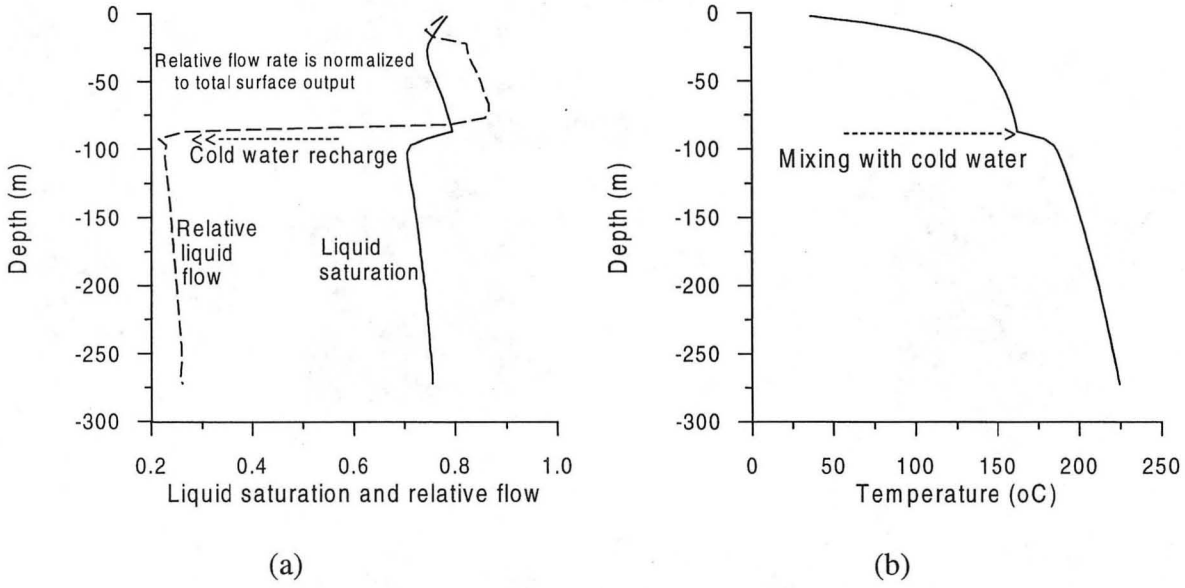

Fig. 3. Liquid saturation and relative flow (a) and temperature (b, in ^{o}C) distribution along the fracture zone.

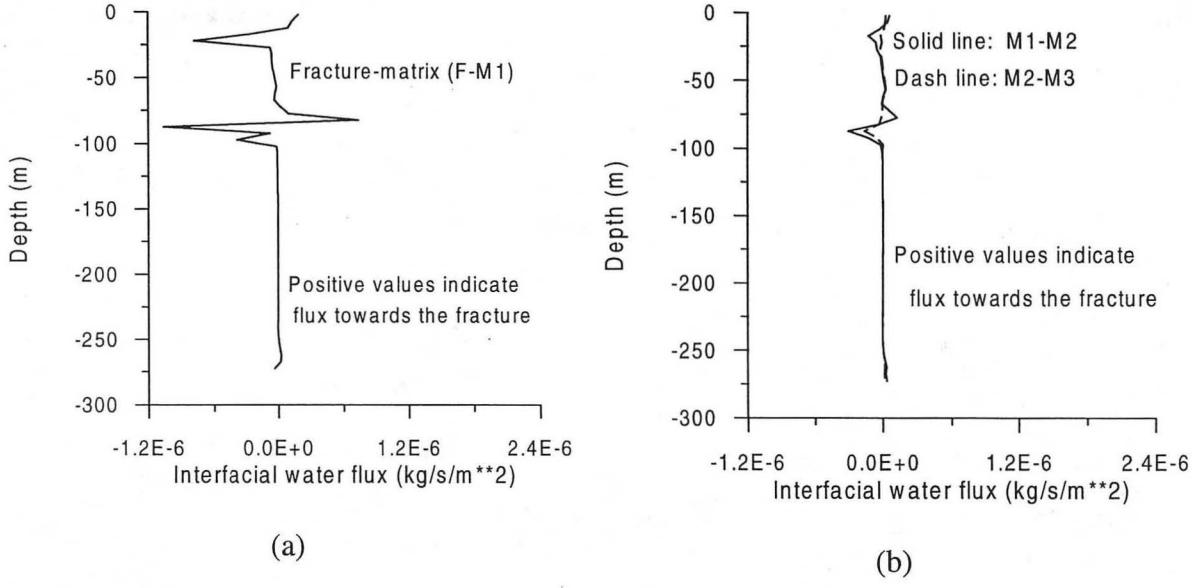

Fig. 4. Interfacial liquid water flux along vertical profiles.

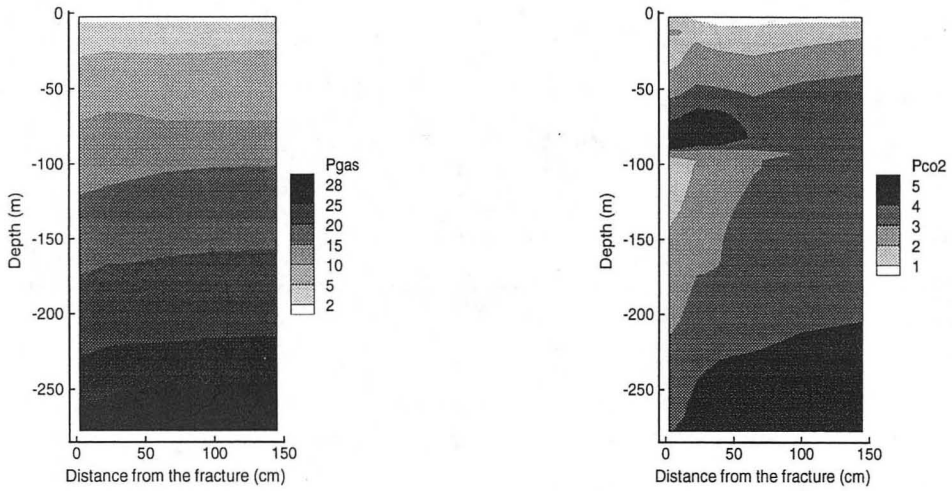

Fig. 5. Gas pressure (in bar) distribution in the fracture-matrix system, (a) total gas phase pressure, (b) CO_2 partial pressure.

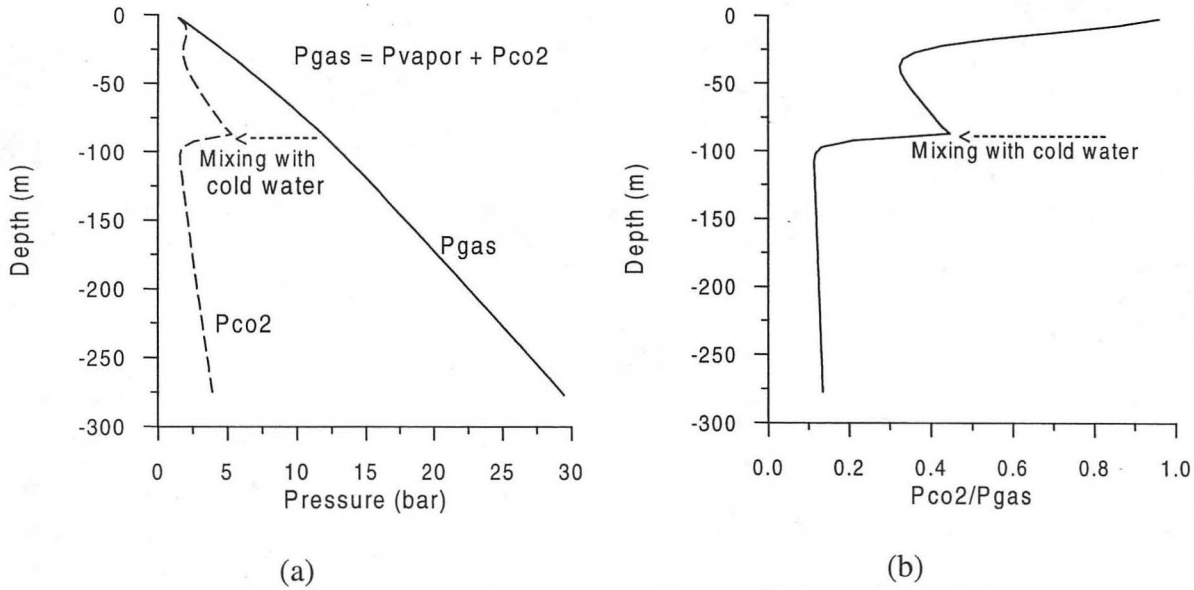

Fig. 6. Gas pressure (bar) along the vertical fracture zone.

4.2. Rock alteration

Results for reactive chemical transport and rock alteration are presented in Figures 7 through 11. The pH distribution (Figure 7a) is generally controlled by CO_2 partial pressure and is modified by mineral dissolution and precipitation. The dissolved silica concentration (in mol/kg H_2O, Figure 7b) decreases from the bottom (close to the heat source) to the top with temperature decreasing, and decreases from the fracture to the inside of the rock matrix. We express rock alteration in terms of a dimensionless change of mineral volume fraction, while the sum of all mineral abundances plus porosity is equal to unity. Sum of changes in mineral abundances and porosity is equal to zero. Negative values of the abundance changes indicate dissolution, while positive indicate precipitation. Changes in the primary mineral abundance after 1000 years are presented in Figure 8. Cristobalite (Figure 8a) and anorthite (Figure 8d) dissolution decrease from the bottom to top with decreasing temperature. After mixing with cold water, their dissolution decreases significantly. Quartz dissolution takes on the same pattern but its value is much smaller than cristobalite in our simulation, as it is in nature. K-feldspar dissolution (Figures 8c) patterns show two peaks, one after the mixing, and the other close to the bottom. Significant dissolution of K-feldspar and albite after the mixing can be clearly seen from the profile along the fracture (Figure 9a). This dissolution peak occurs because: (1) SiO_2(aq), Na, and K concentrations in cold meteoric water (see Table 2) are lower, and (2) solubilities of minerals in the mixed water are much larger than in the cold water (the temperature of the mixture is approximately 160 ^{o}C, and cold water 11 ^{o}C). Unlike the other primary minerals, the bottom albite dissolution peak occurs in the matrix adjacent to the fracture instead of the fracture itself (Figure 8b). A cross-section

for dissolution at a depth of 252.5 m gives a more detailed insight (Figure 9b). Maximum dissolution of albite at the bottom of the section occurs in matrix grid zone M1. The other matrix grid zones (M2-M7) also display significant albite dissolution. In the fracture at this depth, however, albite precipitation occurs rather than dissolution. Albite precipitation in the fractures occurs from the bottom until 235 m depth (Figure 9a). The precipitation is caused by a high Na concentration from the hot water that flows primarily though the fracture, and (2) the dissolved products in the rock matrix that are transported to the fracture zone.

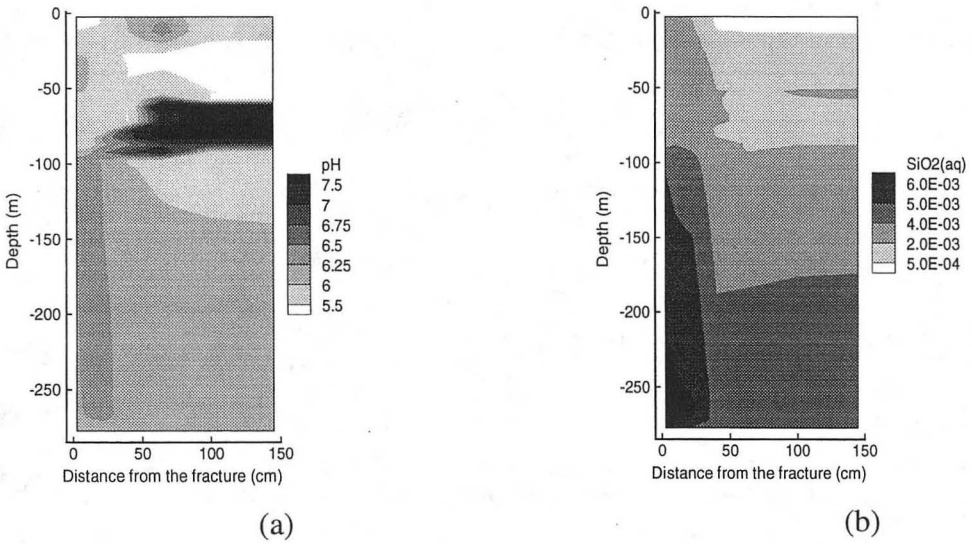

Fig. 7. pH (a) and dissolved silica concentration (b, in mol/kg H_2O) at 1000 years.

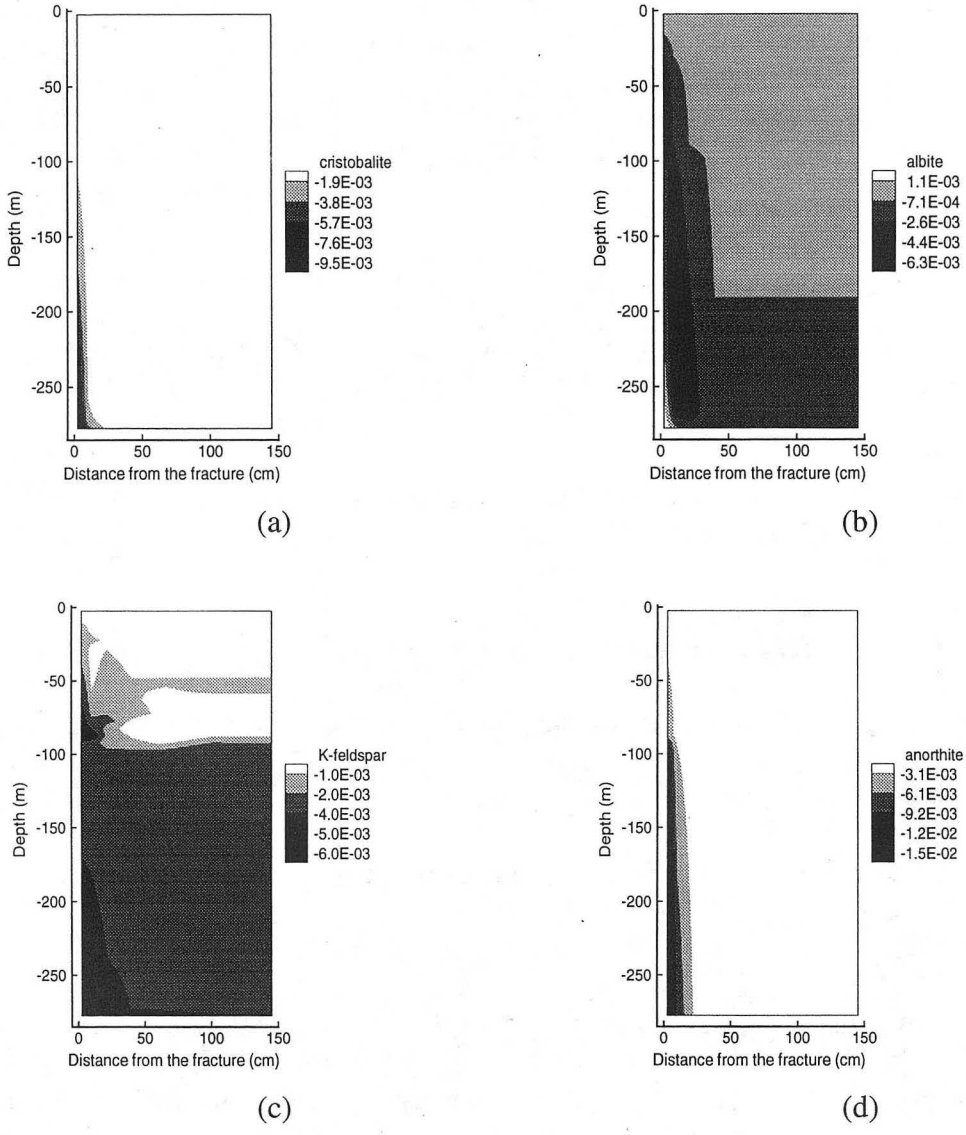

Fig. 8. Change of primary mineral abundance (in volume fraction) after 1000 years.

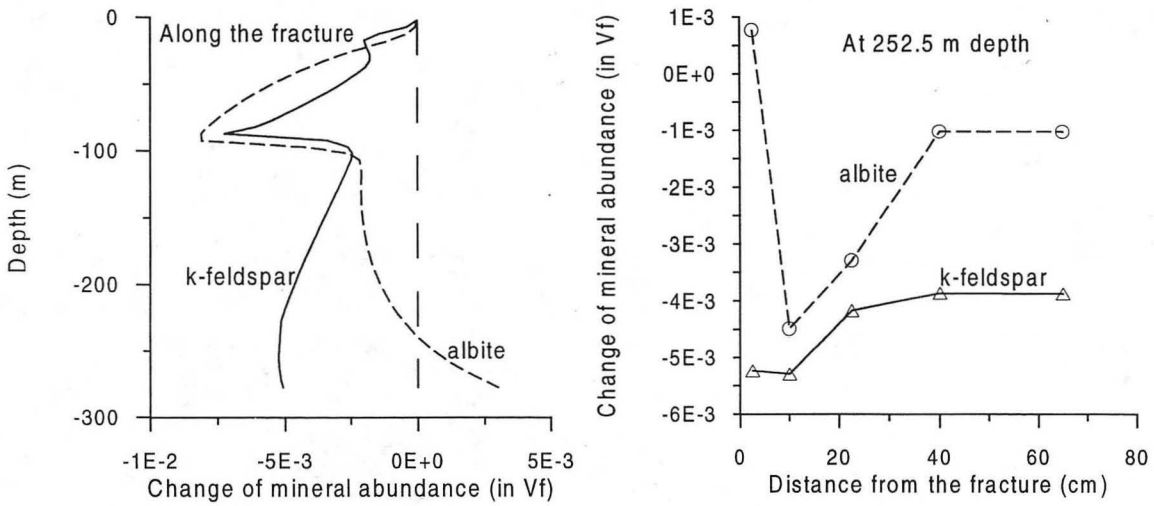

(a) (b)

Fig. 9. Change of primary mineral abundance (in volume fraction) along the fracture (a) and at 252.5 m depth cross-section (b) after 1000 years.

Changes in the secondary mineral abundance are presented in Figure 10. Ca^{2+} released from dissolution of anorthite is taken up by calcite precipitation (Figures 10a, 11a, and 11b). Calcite precipitation decreases from the bottom until the mixing horizon. This is because (1) calcite solubility increases with decreasing temperature, and (2) Ca^{2+} availability decreases because less anorthite dissolves at shallower elevations. Calcite precipitation occurs mainly in the fracture, and gradually decreases away from the fracture in the matrix interior (Figure 11b). Kaolinite precipitation (Figure 10b) occurs mostly in the lower temperature range, and concentrates around the mixing horizon. Muscovite, paragonite, and pyrophyllite (Figures 10c, d and e) are also formed as secondary phases. Precipitation of these three minerals in general decreases from the bottom to the top. Muscovite precipitation is extensive, and decreases gradually from the fracture to the matrix interior. Paragonite and pyrophyllite precipitation occurs mostly along the fracture until the mixing horizon. Finally, some amorphous silica precipitates close to the land surface.

The general picture of changes of porosity in the fracture-matrix system due to mineral dissolution and precipitation is presented in Figure 10f. An increasing porosity (from t=0) close to the heat source can be observed. The maximum increase in porosity appears in the matrix close to the fracture wall and not on the fracture walls. Figure 11b shows that a maximum increase in porosity occurs in M2. This indicates that there is considerable dissolution in the matrix. The dissolved products in the matrix are transported locally by diffusion to the fracture, then the chemical components leached from the matrix are transported upward through the fracture. A significant porosity increase also occurs in the mixing region. Figure 11a show in detail the porosity evolution along the fracture. Three regions of change can be distinguished. A porosity increase occurs close to the heat source (from the bottom to approximately 200 m depth). Then the porosity decreases as the mixing horizon is approached. A larger porosity increase (with a maximum value of 0.8%) occurs after mixing with cold meteoric water. The pattern of porosity change in the fracture suggests that: (1) close to the heat source dissolution dominates over precipitation due to the higher temperature, (2) away from the heat source precipitation dominates, because chemical components transported from the bottom precipitate in a lower temperature environment, and (3) the mixing with cold meteoric water results in an enhanced dissolution.

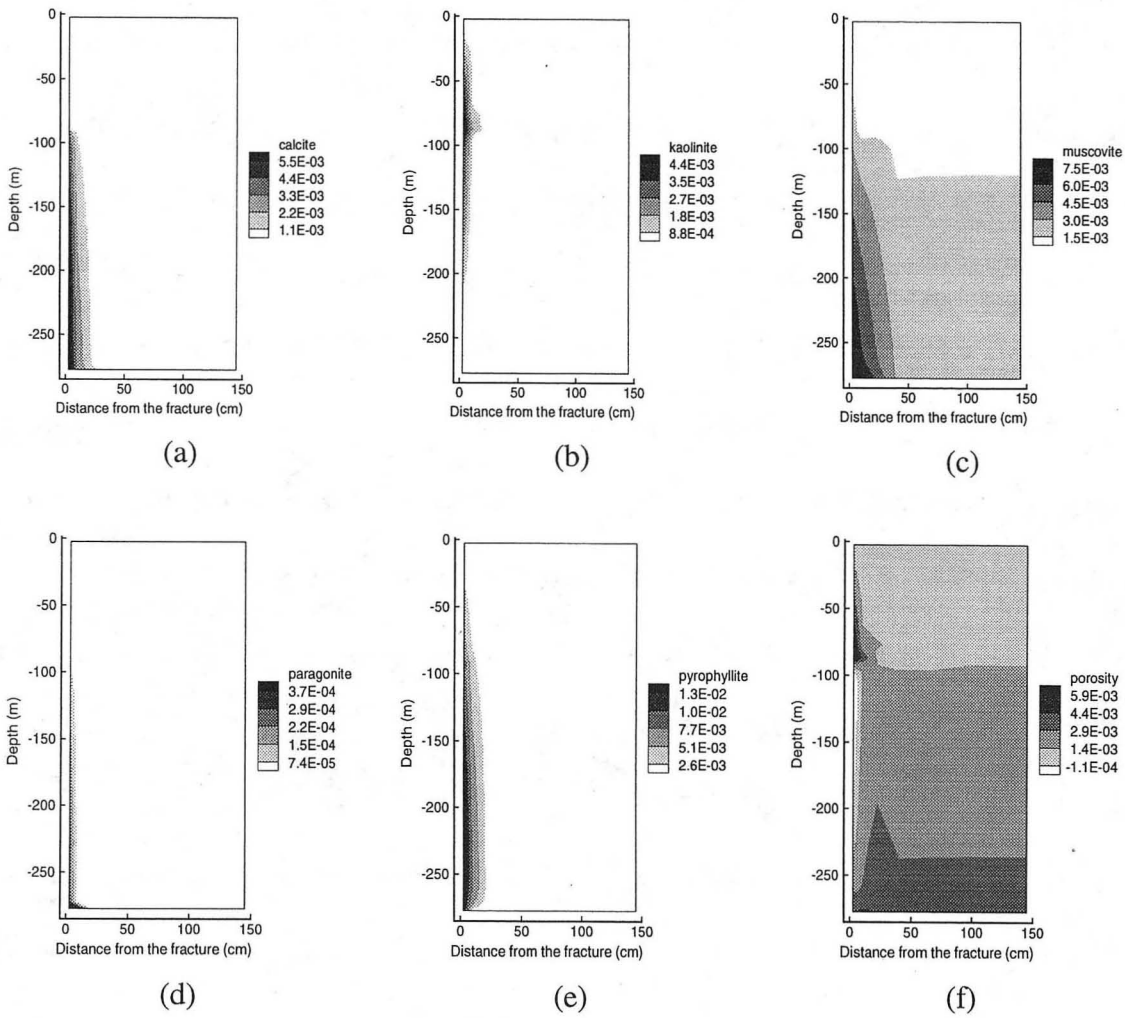

Fig. 10. Change of mineral abundance (secondary phases, in volume fraction) and porosity after 1000 years.

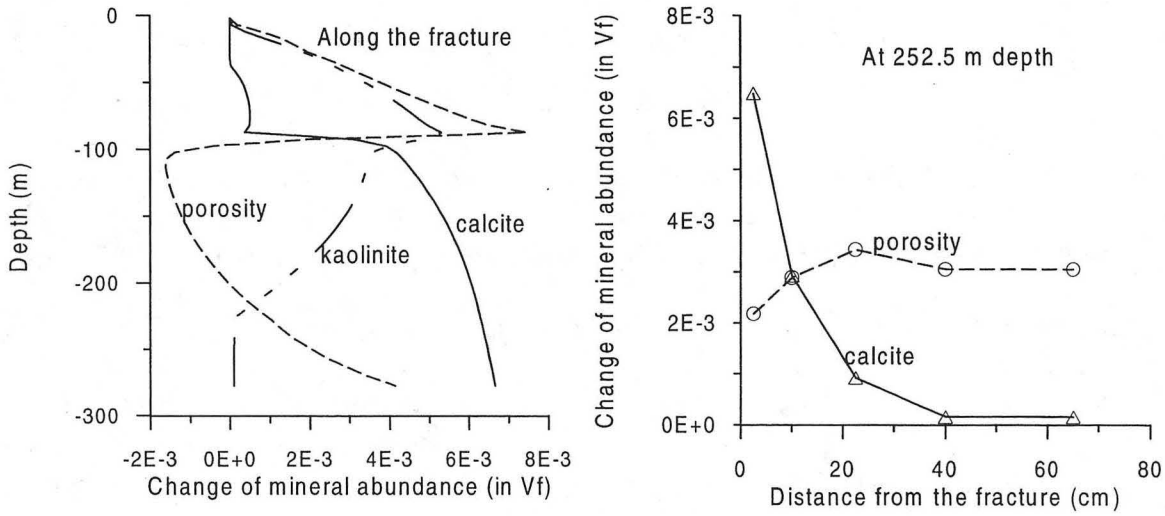

(a) (b)

Fig. 11. Change of mineral abundance (secondary phases, in volume fraction) and porosity along the fracture (a) and at 252.5 m depth cross-section (b) after 1000 years.

4.3. Sensitivity to the surface area

Estimates of field mineral dissolution and precipitation rates cover a wide range of values. Specific reactive surface areas may vary over several orders of magnitude depending on grain size, mineralogy, surface roughness, coatings, weathering, and biological effects [*White and Peterson*, 1990]. For the purpose of analyzing sensitivity, we performed two additional reactive transport simulations by increasing and decreasing the surface areas listed in Table 3 by one order of magnitude. The surface areas for the secondary minerals are changed by the same factors. The surface area evolution in natural geologic media is very complex, especially for multi-mineralic systems, which are not quantitatively described at this time. Nevertheless, this surface area sensitivity analysis gives some general understanding of its impact on the overall behavior of the system.

For the simulation with the surface area increasing, some changes of mineral abundance and porosity are presented in Figure 12. For example, much more albite

dissolution occurs. At the peak (87.25 m depth) albite dissolves almost completely (initial V_f = 2%, where V_f is volume fraction). Close to the bottom, albite dissolution is not significant and the bottom peak almost disappears. There is more K-feldspar and anorthite dissolution (compare Figure 12b to 8c, and Figure 12c to 8d). At the fracture and close to the fracture, anorthite dissolution is almost complete (initial V_f = 2%,) except close to the land surface. Consequently, calcite precipitation is more extensive, particularly in the matrix (compare Figure 12d to Figure 10a). The kaolinite precipitation peak moves upward closer to the land surface (compare Figure 12e to Figure 10b). Porosity changes are much more substantial especially in the matrix (compare Figure 12f to Figure 10f) due to greater dissolution. Below 165 m depth, the porosity increases by about 2%. The porosity at the mixing horizon also increases by 2% (0.8% in the first simulation).

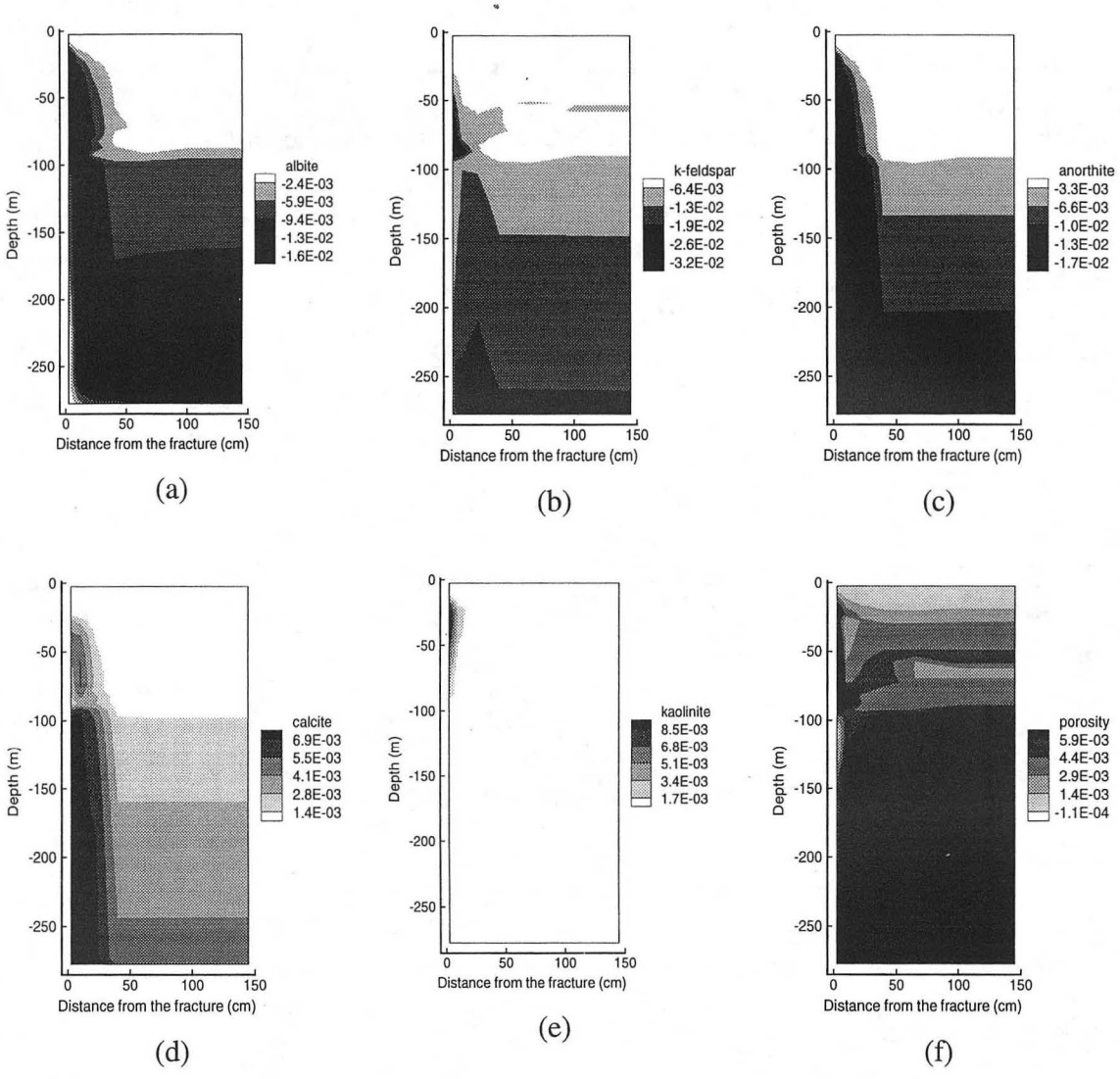

Fig. 12. Change of mineral abundance (in volume fraction) after 1000 years obtained by increasing surface areas (Table 3) by one order of magnitude.

The results obtained by decreasing the surface area by one order of magnitude, are presented in Figure 13. Albite dissolution (Figure 13a) occurs only in the matrix adjacent to the fracture wall and close to the heat source. The K-feldspar and anorthite dissolution patterns (Figure 13b and c) are generally similar to the previous two simulations but

much less dissolution occurs in the matrix. Calcite precipitation (Figure 13d) appears mostly in the fracture. The kaolinite precipitation (Figure 13e) pattern is similar to that in the first simulation. The porosity (Figure 13f) increase in the fracture and close to the fracture is slightly greater than that in the first simulation, while in the matrix porosity increase is smaller than that in the first. This suggests that the reactive surface area reduction results in less mineral dissolution in the matrix, and more in the fracture.

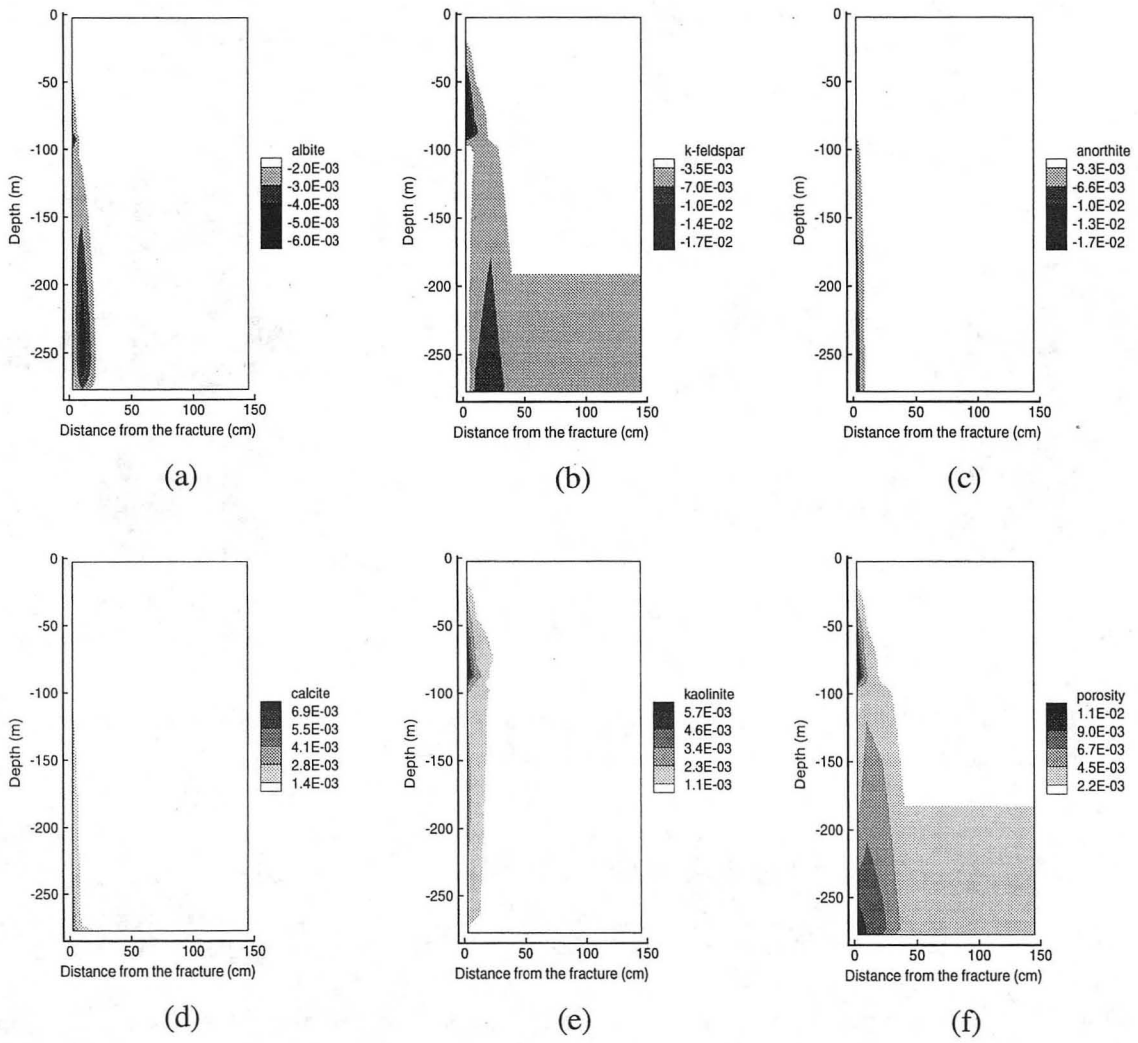

Fig. 13. Change of mineral abundance (in volume fraction) after 1000 years obtained by decreasing surface areas (Table 3) by one order of magnitude.

5. Discussion

The simulated calcite precipitation in the high temperature fracture region is consistent with field observations. For example, calcite is the dominant secondary mineral observed in well cuttings and cores from the LVC hydrothermal fields associated with magmatic activity [*White and Peterson*, 1991]. Calcite precipitation in a fracture may inhibit fluid flow and chemical transport, and stop fracture fluid and chemical exchange with the matrix. These effects are not considered in the present simulation. Kaolinite precipitation occurs mostly in the lower temperature range, and concentrates around the mixing horizon. This pattern is similar to the LVC field observations reported by *Flexser* [1991].

The simulated sharp increase of CO_2 partial pressure after mixing with cold water may be overestimated. This is because in natural hydrothermal systems cold water recharge occurs over a longer depth rather than one grid block (5 m depth) applied in the simulation. In reality, the partial pressure increase may be achieved gradually. In turn, this could affect mineral dissolution and precipitation patterns, and their peak values such as K-feldspar dissolution and kaolinite precipitation could be lower than the simulated values. Consequently, increase of porosity could be reduced. At the land surface, the gas phase is almost entirely made up of CO_2 in the simulation. The intensive CO_2 outflow is frequently observed in hydrothermal fields such as in the LVC [Kennedy, personal comm.].

Because of numerous uncertainties and approximations, numerical simulation results may not completely match field observations of water and gas compositions, and alteration of mineral assemblages. For example, the kinetics of heterogeneous reactions are scale and history-dependent, and cannot be reliably quantified. Reactive surface areas are notoriously uncertain and subject to poorly quantifiable phenomena such as armoring of mineral phases by others. Two-phase flow in fractured rock is affected by multi-scale heterogeneities; the lack of sufficiently detailed characterization data at the field site, as well as the enormous intrinsic variability of two-phase flow in fractures severely limit possibilities for a fully mechanistic description. Variations in water and gas chemistry data could considerably affect rock alteration patterns. Nevertheless, the "numerical experiments" give a detailed view of the dynamical interplay between coupled hydrologic, thermal, and chemical processes, albeit in an approximate fashion. A critical evaluation of modeling results can provide useful insight into process mechanisms such as fracture-matrix interaction, liquid-gas phase partitioning, and conditions and parameters controlling heterogeneous reactions.

6. Concluding remarks

The fracture is the dominant global fluid flow and chemical transport pathway. The matrix serves as a high capacity heat buffer and transfer medium due to its larger volume, and as a local medium for chemical diffusion. Almost all CO_2 is transported through the fracture. Cooling and condensation results in an elevated CO_2 partial pressure. The CO_2 is the dominant gas phase constituent close to the land surface.

Considerable dissolution in the matrix is observed over a 1000 year time period. The dissolved chemical constituents leached from the matrix are transported upward through the fracture. Close to the heat source, dissolution dominates over precipitation, resulting in increasing porosity. Away from the heat source precipitation dominates because chemical constituents, transported from the bottom, precipitate in a lower temperature environment. Mixing with cold and dilute meteoric water also results in enhanced dissolution and porosity increase in this study case.

The predicted alteration of primary rock minerals and the development of secondary mineral assemblages are consistent with field observations such as in LVC. The rock alteration pattern is sensitive to the reactive surface areas which in turn affect the reaction rates. A surface area increase results in more dissolution and more porosity increase in the matrix, while a decrease causes less dissolution in the matrix and slightly enhanced dissolution in the fracture.

The range of problems concerning the interaction of hydrothermal fluids with rocks is very broad. The present simulation results are specific to the reservoir conditions and parameters considered, and water and gas chemistry used in this study. However, the model used may provide a capability for investigating hydro-thermo-chemical alteration in fractured rocks with applications both in fundamental analysis of hydrothermal system and in the exploration of geothermal reservoirs.

Appendix 1. Mathematical equations

All flow and transport equations have the same structure, and can be derived from the principle of mass (or energy) conservation. A detailed mathematical formulation is given in *Xu et al.* [1997]. Table A.1 summarizes these equations and Table A.2 gives the meaning of symbols used. The fluid and heat flow has been discussed in detail by *Pruess* [1987 and 1991]. Aqueous species are subject to transport in the liquid phase as well as to local chemical interactions with the solid and gaseous phases. Transport equations are written in terms of total dissolved concentrations of chemical components which are concentrations of their basis species plus their associated aqueous secondary species [*Yeh and Tripathi*, 1991; *Steefel and Lasaga*, 1994; *Walter et al.*, 1994]. Advection and diffusion processes are considered for chemical transport, and their coefficients are assumed to be the same for all species. The vapor-CO_2 diffusion coefficient is a function of pressure and temperature, and is calculated from the equation given by *Vargaftik* [1975].

Table A.1. Governing equations for fluid and heat flow, and chemical transport. Symbol meanings are given in Table A.2.

General governing equations: $\dfrac{\partial M_\kappa}{\partial t} = -\nabla F_\kappa + q_\kappa$

Water: $M_w = \phi(S_l\rho_l X_{wl} + S_g\rho_g X_{wg})$ $\quad F_w = X_{wl}\rho_l \mathbf{u}_l + X_{wg}\rho_g \mathbf{u}_g$ $\quad q_w = q_{wl} + q_{wg}$

CO_2: $M_c = \phi(S_l\rho_l X_{cl} + S_g\rho_g X_{cg})$ $\quad F_c = X_{cl}\rho_l \mathbf{u}_l + X_{cg}\rho_g \mathbf{u}_g$

$q_c = q_{cl} + q_{cg} + q_{cr}$

Heat: $M_h = \phi(S_l\rho_l U_l + S_g\rho_g U_g) + (1-\phi)\rho_s U_s$ $\quad F_h = \sum_{\beta=l,g} h_\beta \rho_\beta \mathbf{u}_\beta - \lambda\nabla T$ $\quad q_h$

where $\mathbf{u}_\beta = -k\dfrac{k_{r\beta}}{\mu_\beta}\left(\nabla P_\beta - \rho_\beta \mathbf{g}\right)$ $\quad \beta = l, g$ $\quad$ (Darcy's Law)

Chemical components in the liquid phase ($j = 1,2,\ldots,N_l$):

$M_j = \phi S_l C_{jl}$ $\quad F_j = \mathbf{u}_l C_{jl} - (\tau\phi S_l D_l)\nabla C_{jl}$ $\quad q_j = q_{jl} + q_{js} + q_{jg}$

$\tau_\beta = \phi^{1/3} S_\beta^{7/3}$ $\quad$ [*Millington and Quirk*, 1961]

Table A.2. Symbols used in Table A.1.

C	component concentration, mol L^{-1}	ρ	density, kg m^{-3}
D	diffusion coefficient, m^2s^{-1}	μ	viscosity, kg $m^{-1}s^{-1}$
F	mass flux, kg $m^{-2}s^{-1}$ (*)	λ	heat conductivity, W $m^{-1}K^{-1}$
k	permeability, m^2		
k_r	relative permeability	Subscripts:	
g	gravitational acceleration, m s^{-2}	c	CO_2
M	mass accumulation, kg m^{-3}	g	gas phase
N	number of chemical components	h	heat
p	pressure, Pa	j	aqueous chemical component
q	source/sink	l	liquid phase
S	saturation	r	reaction
T	temperature, °C	s	solid phase
U	internal energy, J kg^{-1}	w	water
u	Darcy velocity, m s^{-1}	κ	governing equation index
X	mass fraction	β	phase index
ϕ	porosity	τ	medium tortuosity

(*) For chemical transport and reaction calculations, molar units are used instead of kg.

The primary governing equations given in Table 1 must be complemented with constitutive local relationships that express all parameters as functions of thermophysical and chemical variables. These expressions for non-isothermal multiphase flow are given by *Pruess* [1987]. The expressions for chemical reactions are given in *Xu et al.* [1997]. Aqueous complexation, acid-base, gas dissolution/exsolution are considered under the local equilibrium assumption. Mineral dissolution/precipitation can be subject either to local equilibrium or to kinetic conditions. Thermodynamic and kinetic data are functions of temperature, which are solved from fluid and heat flow equations. The formulation of chemical equilibrium is similar to that by *Parkhurst* [1980], *Reed* [1982], *Yeh and Tripathi* [1991], *Wolery* [1992], and *Steefel and Lasaga* [1994]. For kinetically-controlled mineral dissolution and precipitation, a general form of rate law [*Lasaga*, 1984; and *Steefel and Lasaga*, 1994] are used

$$r_m = A_m k_m \left[1 - \left(\frac{Q_m}{K_m}\right)^{\mu}\right]^n \qquad (A.1)$$

where m is mineral index, r_m is the dissolution/precipitation rate (positive values indicate dissolution, and negative values precipitation), A_m is the specific reactive surface area per kg H_2O, k_m is the rate constant (moles per unit mineral surface area and unit time) which is temperature dependent, K_m is the equilibrium constant for the mineral-water reaction written for the destruction of one mole of mineral m, Q_m is ion activity product, The parameters μ and n are two positive numbers normally determined by experiment, and are usually, but not always, taken equal to unity. The temperature dependence of the reaction rate constant can be expressed reasonably well via an Arrhenius equation [*Lasaga*, 1984; and *Steefel and Lasaga*, 1994]. Since many rate constants are reported at 25 °C, it is convenient to approximate rate constant dependency as a function of temperature, thus

$$k = k_{25} \exp\left[\frac{-E_a}{R}\left(\frac{1}{T} - \frac{1}{298.15}\right)\right] \qquad (A.2)$$

where E_a is the activation energy, k_{25} is the rate constant at 25 °C, R is gas constant, T is absolute temperature.

Equilibria involving aqueous and gaseous species are assumed to obey the mass-action law (MAL). For example, for CO_2 gas dissolution, $CO_2(g) = CO_2(aq)$, we have

$$K_{CO_2(g)} \Gamma_{CO_2(g)} P_{CO_2(g)} = c_{CO_2(aq)} \qquad (A.3)$$

where K is the equilibrium constant, and Γ is the fugacity coefficient. At low pressures (in the range of atmospheric pressure), the gaseous species are assumed to behave as an ideal mixture, and the fugacity coefficient is assumed equal to unity. At higher temperatures and pressures, such as boiling conditions in hydrothermal systems, as

applies to the conditions presented in this paper, the assumption of ideal gas and ideal mixing behavior is not valid, and the fugacity coefficients should be corrected according to temperatures and pressures of the study system [*Spycher and Reed*, 1988]. For the present H_2O-CO_2 mixture with boiling conditions, we assume that H_2O and CO_2 are real gases, but ideal mix. According to *Spycher and Reed* [1988], the fugacity coefficients can be calculated from

$$\ln\Gamma = \left(\frac{a}{T^2} + \frac{b}{T} + c\right)P + \left(\frac{d}{T^2} + \frac{e}{T} + f\right)\frac{P^2}{2} \qquad (A.4)$$

where P is the total gas pressure (vapor and CO_2), T is absolute temperature, and a, b, c, d, e, and f are constants fitted from experimental data. For P-T ranges, 50-350 °C, up to 500 bars, the fitted constants have the following values: a = -1430.87, b = 3.598, c = -2.27376×10^{-3}, d = 3.47644, e = -1.04247×10^{-2}, and f = 8.46271×10^{-6}. Examples of equilibrium calculations between aqueous and gas phases show that ideal mixing of real gases is an adequate approximation in the above-mentioned P-T ranges [*Spycher and Reed*, 1988].

Acknowledgement. We thank John Apps for helpful discussions and suggestions. We are grateful to Nicolas Spycher, Mack Kennedy, Curtis Oldenburg, Steve White, and Daniel Swenson for a review of the manuscript and suggestions for improvement. This work was supported by the Laboratory Directed Research and Development Program of the Ernest Orlando Lawrence Berkeley National Laboratory, and by the Assistant Secretary for Energy Efficiency and Renewable Energy, Office of Geothermal and Wind Technologies, of the U.S. Department of Energy, under Contract No. DE-AC03-76SF00098.

References

Battistelli, A., Calore, C., and Pruess, K. (1997). The Simulator TOUGH2/EWASG for Modeling Geothermal Reservoirs with Brines and Non-Condensible Gas. *Geothermics*, Vol. 26 (4), pp.437-464.

Bolton, E. W., A. C. Lasaga, and D. M. Rye, Long-term flow/chemistry feedback in a porous medium with heterogenous permeability: Kinetic control of dissolution and precipitation, *Am. J. Sci.*, 299, 1-68, 1999.

Friedly, J.C., and J. Rubin, Solute transport with multiple equilibrium controlled or kinetically controlled chemical reactions. *Water Resour. Res.*, 28, 1935-1953, 1992.

Flexser, S., Hydrothermal alteration and past and present thermal regimes in the western moat of Long Valley Cadera (California), *J. Volcanol. and Geotherm. Res.*, 48, 303-318, 1991.

Johnson J. W., K. G. Knauss, W. E. Glassley, L. D. Deloach, A. F. B. Tompson, Reactive transport modeling of plug-flow reactor experiments: Quartz and tuff dissolution at 240°C. *J. Hydrol.*, 209, 81-111, 1998.

Lasaga, A. C., Chemical kinetics of water-rock interactions, *J. Geophys. Res.*, v. 89, 4009-4025, 1984.

Millington, R. J., and J. P. Quirk, Permeability of porous solids, Trans. Faraday Soc., 57, 1200-1207, 1961.

Moller, N., J. P. Greenberg, and J. H. Weare, Computer modeling for geothermal systems: Predicting carbonate and silica scale formation, CO_2 breakout and H_2S exchange, *Transport in Porous Media*, 33, 173-204, 1998.

Narasimhan, T. N., and P. A. Witherspoon, An integrated finite difference method for analyzing fluid flow in porous media, *Water Resour. Res.*, 12, 57–64, 1976.

Ohmoto, H., and A. C. Lasaga, Kinetics of reaction between aqueous sulfates and sulfides in hydrothermal systems. *Geochim. Cosmochim. Acta*, 46, 1727-1746, 1982.

Parkhurst, D. L., D. C. Thorstenson, and L. N. Plummer, PHREEQE: A computer program for geochemical calculations, US Geol. Surv. Water Resour. Invest. 80-96, 174 pp., 1980.

Pruess, K., TOUGH user's guide, Nuclear Regulatory Commission, report NUREG/CR-4645 (also Lawrence Berkeley Laboratory Report LBL-20700, Berkeley, California), 1987.

Pruess, K., TOUGH2: A general numerical simulator for multiphase fluid and heat flow, Lawrence Berkeley Laboratory Report LBL-29400, Berkeley, California, 1991.

Raffensperger, J. P., Numerical simulation of sedimentary basin-scale hydrochemical processes, In Advances in Porous Media, Corapcioglu, Y. C., (ed.), Amsterdam, The Netherlands, Elsevier Science, 440 pp., 1996.

Reed, M. H., Calculation of multicomponent chemical equilibria and reaction processes in systems involving minerals, gases and aqueous phase, *Geochimica et Cosmochimica Acta*, 46, 513-528, 1982.

Sorey, M. L., Evolution and present state of the hydrothermal system in Long Valley Cadera, *J. Geophys. Res.*, 90, 11219-11228, 1985.

Spycher, N. F., and M. H. Reed, Fugacity coefficients of H_2, CO_2, CH_4, H_2O and of H_2O-CO_2-CH_4 mixtures: A virial equation treatment for moderate pressures and temperatures applicable to calculations of hydrothermal boiling, *Geochimica et Cosmochimica Acta*, 52, 739-749, 1988.

Spycher, N. F., and M. H. Reed, Evolution of a broadlands-type epithermal ore fluid along alternative P-T paths: Implications for the transport and deposition of base, precious, and volatile metals, *Economic Geology,* 84, 328-359, 1989.

Steefel, C. I., and P. van Cappellen, A new kinetic approach to modeling water-rock interaction: The role of nucleation, precursors and Ostwald ripening, *Geochim. Cosmochim. Acta*, 54, 2657-2677, 1990.

Steefel, C. I., and A. C. Lasaga, A coupled model for transport of multiple chemical species and kinetic precipitation/dissolution reactions with applications to reactive flow in single phase hydrothermal system, *Am. J. Sci.*, 294, 529-592, 1994.

Van Genuchten, M. T., A closed-form equation for predicting the hydraulic conductivity of unsaturated soils, Soil Sci. Soc. Am. J., 44, 892-898, 1980.

Vargaftik, N. B., Tables on the thermophysical properties of liquids and gases, Second edition, John Wiley and Sons, New York, 1975.

Verma, A., and K. Pruess, Thermohydrological conditions and silica redistribution near high-level nuclear wastes emplaced in saturated geological formations, *Journal and Geophysical Research*, 93, 1159-1173, 1988.

Walter, A. L., E. O. Frind, D. W. Blowes, C. J. Ptacek, and J. W. Molson, Modeling of multicomponent reactive transport in groundwater, 1, Model development and evaluation, *Water Resour. Res.*, 30, 3137-3148, 1994.

White, S. P., Multiphase non-isothermal transport of systems of reacting chemicals, *Water Resour. Res.*, 31, 1761-1772, 1995.

White, S. P., and B. W. Christenson, Modeling the Alteration Halo of a Diorite Intrusion, New Zealand Geothermal Congress, 1998.

White, S. P., and E. K. Mroczek, Permeability changes during the evolution of a geothermal field due to the dissolution and precipitation of quartz, *Transport in Porous Media*, 33, 81-101, 1998.

White, A. F., and M. L. Peterson, Role of reactive surface area characterization in geochemical models, In Chemicals Models of Aqueous Systems 2, Amer. Chem. Soc. Symp. Ser., 461-475, 1990.

White, A. F., and M. L. Peterson, Chemical equilibrium and mass balance relationships associated with Long Valley hydrothermal system, California, USA, *J. Volcanol. and Geotherm. Res.*, 48, 283-302, 1991.

Wolery, T. J., EQ3/6: Software package for geochemical modeling of aqueous systems: Package overview and installation guide (version 7.0), Lawrence Livermore National Laboratory Report UCRL-MA-110662 PT I, Livermore, California, 1992.

Xu, T., F. Gérard, K. Pruess, and G. Brimhall, Modeling non-isothermal multiphase multi-species reactive chemical transport in geologic media, Lawrence Berkeley National Laboratory Report LBNL-40504, Berkeley, California, 79 pp., 1997.

Xu, T., and K. Pruess, Coupled modeling of non-isothermal multiphase flow, solute transport and reactive chemistry in porous and fractured media: 1. Model development and validation, Lawrence Berkeley National Laboratory Report LBNL-42050, Berkeley, California, 38 pp., 1998.

Xu, T., J. Samper, C. Ayora, M. Manzano, and E. Custodio, Modeling of non-isothermal multi-component reactive transport in field-scale porous media flow system, *J. Hydrol.*, 214, 144-164, 1999a.

Xu, T., K. Pruess, and G. Brimhall. An improved equilibrium-kinetics speciation algorithm for redox reactions in variably saturated flow systems, *Computers & Geosciences,* 25, 655-666, 1999b.

Yeh, G. T., and V. S. Tripathi, A model for simulating transport of reactive multispecies components: model development and demonstration, *Water Resour. Res.*, 27, 3075-3094, 1991.

ERNEST ORLANDO LAWRENCE BERKELEY NATIONAL LABORATORY
ONE CYCLOTRON ROAD | BERKELEY, CALIFORNIA 94720

Prepared for the U.S. Department of Energy under Contract No. DE-AC03-76SF00098